Silicalite-1 Layer Secures the Bifunctional Nature of a CO_2 Hydrogenation Catalyst

Shiyou Xing, Savannah Turner, Donglong Fu, Sophie van Vreeswijk, Yuanshuai Liu, Jiadong Xiao, Ramon Oord, Joachim Sann, and Bert M. Weckhuysen*

Cite This: *JACS Au* 2023, 3, 1029−1038

Read Online

ACCESS | Metrics & More | Article Recommendations | Supporting Information

ABSTRACT: Close proximity usually shortens the travel distance of reaction intermediates, thus able to promote the catalytic performance of CO_2 hydrogenation by a bifunctional catalyst, such as the widely reported In_2O_3/H-ZSM-5. However, nanoscale proximity (*e.g.*, powder mixing, PM) more likely causes the fast deactivation of the catalyst, probably due to the migration of metals (*e.g.*, In) that not only neutralizes the acid sites of zeolites but also leads to the reconstruction of the In_2O_3 surface, thus resulting in catalyst deactivation. Additionally, zeolite coking is another potential deactivation factor when dealing with this methanol-mediated CO_2 hydrogenation process. Herein, we reported a facile approach to overcome these three challenges by coating a layer of silicalite-1 (S-1) shell outside a zeolite H-ZSM-5 crystal for the In_2O_3/H-ZSM-5-catalyzed CO_2 hydrogenation. More specifically, the S-1 layer (1) restrains the migration of indium that preserved the acidity of H-ZSM-5 and at the same time (2) prevents the over-reduction of the In_2O_3 phase and (3) improves the catalyst lifetime by suppressing the aromatic cycle in a methanol-to-hydrocarbon conversion step. As such, the activity for the synthesis of C_2^+ hydrocarbons under nanoscale proximity (PM) was successfully obtained. Moreover, an enhanced performance was observed for the S-1-coated catalyst under microscale proximity (*e.g.*, granule mixing, GM) in comparison to the S-1-coating-free counterpart. This work highlights an effective shielding strategy to secure the bifunctional nature of a CO_2 hydrogenation catalyst.

KEYWORDS: silicalite-1 shielding effect, bifunctional nature, CO_2 hydrogenation, zeolite
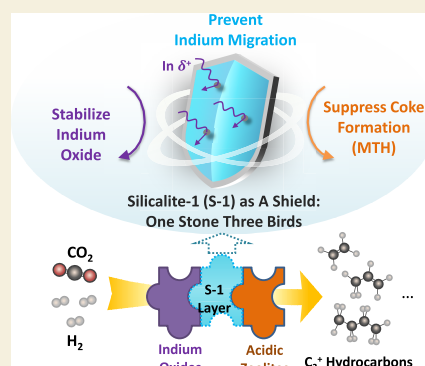
INTRODUCTION

Valorizing CO_2 with renewable H_2 by heterogeneous thermocatalysis is a promising route to abate the issue of global warming. CO_2 hydrogenation also offers a set of innovative fossil-free approaches for the synthesis of chemicals and fuels,[1−3] including C_1 molecules, such as CO,[4−6] CH_4,[7,8] formate and formic acid,[9,10] methanol,[11−13] and C_2^+ hydrocarbons, like lower olefins,[14,15] aromatics,[16,17] or even gasoline fuel ingredients.[18,19] In view of the demand for hydrocarbon fuels in the next decades for long-distance transportation, especially for the aviation sector,[20] enhancing the carbon–carbon coupling chemistry over direct CO_2 hydrogenation is therefore of great importance. To reach this goal, at least two attractive routes to date have been reported. The first one is converting CO_2 to CO *via* the reverse water-gas-shift (RWGS) reaction followed by the Fischer–Tropsch synthesis (FTS) process over, *e.g.*, an iron-based FTS catalyst material.[21] The second approach utilizes a bifunctional catalyst, in which a metal oxide catalyzes CO_2 to methanol (CTM), which subsequently transforms into hydrocarbons over an acid functionality dispersed within a zeolite material through the so-called methanol-to-hydrocarbon (MTH) process.[22] Because the propagation process for carbon chain formation takes place

within the zeolite framework, bifunctional catalyst materials show a huge capacity in tuning the product selectivity, particularly known for its breaking of the Anderson–Schulz–Flory (ASF) limitation that is commonly found for FTS processes.[23]

The activity of the methanol synthesis catalysts, *e.g.*, metals/metal oxides, and its spatial distance with the acid catalysts are the two determining factors for the overall performance of bifunctional catalyst systems.[24,25] A wealth of research has been performed to explore the combination of methanol synthesis catalysts with zeolites for coupling the catalytic functionalities for CO_2 hydrogenation and carbon–carbon coupling chemistry.[16−18,22,26−29] In_2O_3 or In-based oxides exhibited a superior efficiency in converting CO_2 to methanol, which is ascribed to the formation of abundant surface oxygen vacancies (OVs) due to the high reducibility of the
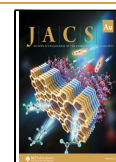
material.[18,30−32] It is believed that a close distance can markedly boost the overall efficiency for carbon−carbon coupling, i.e., C_2^+ synthesis, due to the facilitated transfer of the reaction intermediates.[23,27,33−35] Therefore, one would expect that powder mixing (PM) should perform better than the granule mixture (GM), as the former offers closer proximity between metal oxides and zeolites (Figure 1a).
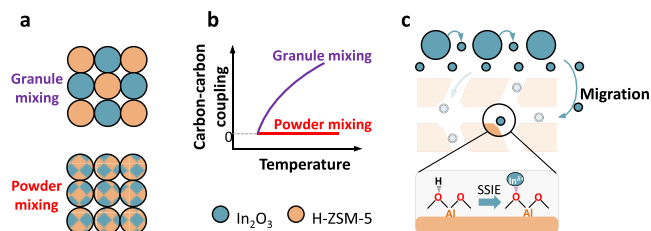

Figure 1. (a) Illustrations of the granule-mixed (GM) and powder-mixed (PM) In_2O_3/H-ZSM-5 bifunctional catalyst systems and (b) the resulting carbon−carbon coupling efficiency as a function of the reaction temperature. (c) Illustration of the proposed mechanism for the zero carbon−carbon coupling efficiency in the PM form, i.e., the migration of indium species followed by solid-state ion exchange (SSIE) with acid sites that may explain the deactivation of the zeolite-based catalysts.

However, unlike other metals, the close proximity of indium-based bifunctional catalyst materials by PM often leads to a complete loss of activity for carbon−carbon coupling (Figure 1b).[18] This is likely due to the migration of indium species under reaction conditions that neutralizes the Brønsted acid sites of zeolites[14,36,37] (Figure 1c) and thus prohibits the carbon−carbon coupling. A similar observation was also reported in the Na-Fe_3O_4/H-ZSM-5-catalyzed CO_2 hydrogenation process.[19] Physical separation of these two active components by, for example, a dual-bed design could be able to suppress the contamination of metal oxides on zeolites; a demerit was then the poor performance due to the increased distance for methanol transfer. Additionally, zeolite coking could be another potential deactivation factor for such an MTH-involved bifunctional catalysis process in practical application scenarios,[31,38] although during CO_2 hydrogenation, long-term (∼100 h) stability was usually observed in lab-scale research.[18,27]

Zeolitic core−shell structures often provide versatile beneficial functions for catalysis,[39,40] for instance, shape selectivity,[41,42] bifunctionality,[43] and sintering resistance.[44,45] Rimer et al. have developed abundant types of core−shell and egg-shell zeolite catalysts that showed enhanced performance in hydrocarbon processing as well as biomass conversion.[46,47] Very recently, the core−shell zeolite has also been reported for CO_2 conversion, primarily for the regulation of the selectivity of aromatic products.[17,48] Herein, we report that such a core−shell zeolite structure was able to overcome the challenges aforementioned during CO_2 hydrogenation, where the construction of the shell, referring to coating a layer of silicalite-1 (S-1) over a pristine zeolite H-ZSM-5 crystal, was realized by a facile secondary growth. Such an S-1 shell was found to be able to secure the bifunctional nature of a typical CO_2 hydrogenation catalyst, i.e., In_2O_3/H-ZSM-5, by which the activity for the synthesis of C_2^+ hydrocarbons under both nanoscale (in a manner of PM) and microscale (in a manner of GM) proximity was well-improved. Multiple benefits from this S-1 shell included (1) suppressing indium contamination on

the acidic zeolite, (2) concurrently keeping the In_2O_3 fraction from being over-reduced, and (3) increasing the overall lifetime of the MTH reactions involved in this bifunctional catalysis system by suppressing coke formation in zeolites.

RESULTS AND DISCUSSION

Characterization of Catalytic Materials

The metal oxide of In_2O_3 was prepared according to the work of the research group of Sun, revealing particle sizes of ca. 20−30 nm (Figure S1). The S-1-coated zeolite (denoted as HZ5-45-S) was prepared based on an H-ZSM-5 material with a Si/Al ratio of 45 (denoted as HZ5-45) using the secondary growth method. High-angle annular dark-field−scanning transmission electron microscopy (HAADF−STEM), high-resolution transmission electron microscopy (HRTEM), and Al energy-dispersive X-ray spectroscopy (EDX) measurements showed that the growth of a crystallized S-1 layer outside the pristine zeolite was successful with a shell thickness of ca. 100−150 nm (Figure 2 and Figure S2). The highest Al content at
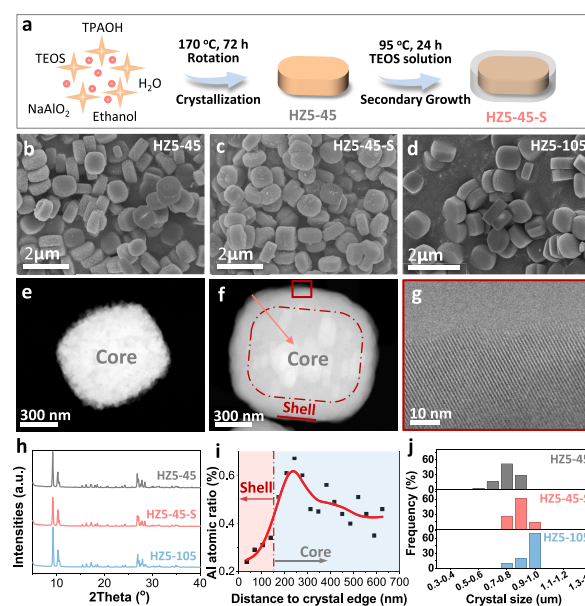

Figure 2. (a) Schematic approach for the synthesis of S-1-coated zeolite. (b−d) Scanning electron microscopy (SEM) images of (b) HZ5-45, (c) HZ5-45-S, and (d) HZ5-105. (e,f) High-angle annular dark-field−scanning transmission electron microscopy (HAADF−STEM) images of (e) HZ5-45 and (f) HZ5-45-S with a rounded rectangle shape to indicate the interface of the S-1 shell and pristine core zeolite. (g) High-resolution transmission electron microscopy (HRTEM) image of the edge of the S-1 shell, indicating a crystallized shell structure. (h) X-ray diffraction (XRD) patterns of three zeolites, showing the same MFI structure. (i) Energy-dispersive X-ray (EDX) spectroscopy of Al atomic ratios across the S-1-coated zeolite crystal in (f) marked with a pink arrow, showing a volcano-type pattern with a low Al ratio in the shell. (j) Crystal size distributions of the three zeolites varying from ca. 0.7 to 0.9 μm.

the core−shell interface (Figure 2i) probably originated from the parent zeolite crystal that possessed an Al-rich surface[49] (Table 1 and Figure S3). Furthermore, pyridine was used to probe the pore connectivity between the shell and core as pyridine shares a slightly smaller spatial size with the MFI pore channel.[50] The results of pyridine adsorption experiments (Figure S4) demonstrated good connectivity between the shell

Table 1. Textural and Acidic Characteristics of the Prepared Zeolite H-ZSM-5 Materials

sample	Si/Al ratio[a]	Si/Al ratio[b]	BET (m²/g)[c]	V_{micro} (cm³/g)[d]	V_{total} (cm³/g)[e]	acidity (mmol/g)[f]			
						weak	strong	total	B/L[g]
HZ5-45	56	44	493	0.16	0.17	0.15	0.24	0.39	4.24
HZ5-45-S	109	363	518	0.17	0.19	0.06	0.12	0.18	2.98
HZ5-105	124	98	413	0.14	0.17	0.05	0.11	0.16	3.03

[a]Achieved by inductively coupled plasma-atomic emission spectroscopy (ICP-AES). [b]Acquired by X-ray photoelectron spectroscopy (XPS). [c]Obtained by the BET method. [d]Calculated by the *t*-plot method. [e]Acquired by single-point adsorption at $p/p°$ of *ca.* 0.96. [f]Calculated by ammonium-temperature programmed desorption (NH₃-TPD). [g]Determined by pyridine-infrared (IR) spectroscopy, with B/L meaning the ratio of Brønsted and Lewis acid site amounts.

and the core crystal. As expected, the S-1 coating caused a decrease in the acidity compared to the pristine zeolite material, more specifically *ca.* 2.2 times lower in the acid amount (Table 1 and Figure S5a). To better illustrate the shell effect, we have synthesized another zeolite H-ZSM-5 (further denoted as HZ5-105) to keep the acid density comparable with that of HZ5-45-S (Table 1 and Figure S5a). Scanning electron microscopy (SEM, Figure 2b−d) results showed that all three zeolites were uniformly distributed with a similar round coffin-like morphology and comparable crystal sizes of *ca.* 0.7 to 0.9 μm (Figure 2j). X-ray diffraction (XRD) and argon physisorption measurements indicated that they shared the same MFI geometry structure (Figure 2h) and a close porosity (Table 1 and Figure S5b). Briefly, by controllable synthesis, three zeolite H-ZSM-5 materials with comparable morphology, porosity, and acidity were made.

Comparison of Catalytic Performance

As the acid sites of the zeolite materials are exclusively responsible for the carbon−carbon coupling, C_2^+ synthesis efficiency (*i.e.*, the space−time yield, STY) could be considered as the descriptor for the activity of zeolites. Knowing the comprehensive study by Gao *et al.* on the optimizations of the reaction conditions,[18] here, we focused on the comparison of the performance difference of these catalyst materials. The mass ratio of In_2O_3 and zeolite was set as 1:1 as it can be seen in Gao's work that it did not show too much difference in the performance when varying this parameter.[18] We first explored the catalytic performance under the PM manner, as shown in Figure 1a. No C_2^+ product (Figure 3a−c) but a high CO selectivity was observed for the In_2O_3/HZ5-45-PM and In_2O_3/HZ5-105-PM materials at all temperatures tested, while the formation of oxygenates (*i.e.*, methanol and dimethyl ether (DME), Table S1) indicated that In_2O_3 was active for the CTM process. These results demonstrated that the zeolite fractions of HZ5-45 and HZ5-105 have all been deactivated.[14,18] In contrast, the catalyst In_2O_3/HZ5-45-S-PM showed an apparent activity for C_2^+ hydrocarbon synthesis (Figure 3b and Figure S6 for the details of these C_2^+ hydrocarbons), reaching an STY of *ca.* 1.0 mmol/g_{oxide}/h under a similar CO_2 conversion (Figure 3a). Tests of the reaction at other temperatures also indicated the production of C_2^+ hydrocarbons (Figure 3d), whose STY values were over 50 times higher than the reported In_2O_3/zeolite catalyst materials under the same PM case (Figure S7). These results demonstrated that the zeolite HZ5-45-S remained active, probably owing to the existence of the S-1 shell. We then applied this strategy to the commercialized zeolite (*i.e.*, CBV8014, with Si/Al = 40) with a nonuniform morphology (Figure S8a), in which only the S-1-coated CBV8014 was found to be able to catalyze carbon−carbon coupling under the
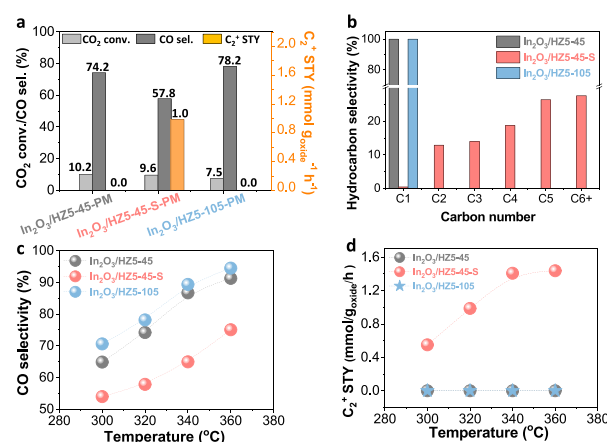

Figure 3. (a−d) CO_2 hydrogenation performance of (a) CO_2 conversion, CO selectivity, and C_2^+ space−time yield (STY) over In_2O_3/HZ5-45-PM, In_2O_3/HZ5-45-S-PM, and In_2O_3/HZ5-105-PM, (b) hydrocarbon distributions, (c) CO selectivity, and (d) C_2^+ STY as a function of reaction temperature. The data for the selectivity of oxygenates including methanol and DME are shown in Table S1. Reaction conditions: $Ar/CO_2/H_2 = 1/6/18$, the mass of two components: 0.5 g of In_2O_3 + 0.227 g of HZ5-45, 0.5 g of In_2O_3 + 0.5 g of HZ5-45-S, 0.5 g of In_2O_3 + 0.5 g of HZ5-105, 320 °C, 2 MPa, and gas hourly space velocity (GHSV) = 3600 mL/g_{oxide}/h; all the reaction data here were collected after 5 h of running.

PM case (Figure S8b−d). Furthermore, the core−shell zeolite showed superior performance of C_2^+ synthesis compared to the S-1 layer-free counterpart material under the GM case (Figure S9a−d).

Restraining the Migration of Indium

To demonstrate the role of the S-1 layer introduced in the bifunctional catalyst materials, we first studied the spent In_2O_3/HZ5-45-PM to unravel the deactivation mechanism. NH₃-TPD analysis (Figure 4a) showed a sharp decrease of acidity in the used In_2O_3/HZ5-45 catalyst in both the weak (125−250 °C) and strong (275−400 °C) acid regions.[36] Electron microscopy characterizations clearly showed the presence of indium species (e.g., the HAADF−STEM EDX mapping on cross-sectional samples in Figure 4b,c) or small nanoparticles (e.g., TEM images in Figure S10a,b) inside the HZ5-45 crystal, thus directly pointing to the reason of deactivation, namely, the contamination from indium species.[14] Specifically, we found that the ratio of indium species was proportional to that of aluminum (Figure S11 and Figure 4f), suggesting that indium species were prone to migrate toward the Al sites, *i.e.*, the acid sites. To confirm this, we have prepared a catalyst 10 wt % indium-impregnated H-ZSM-5 (CBV 8014, with Si/Al = 40, see the synthesis procedure in the Supporting Information). In this catalyst
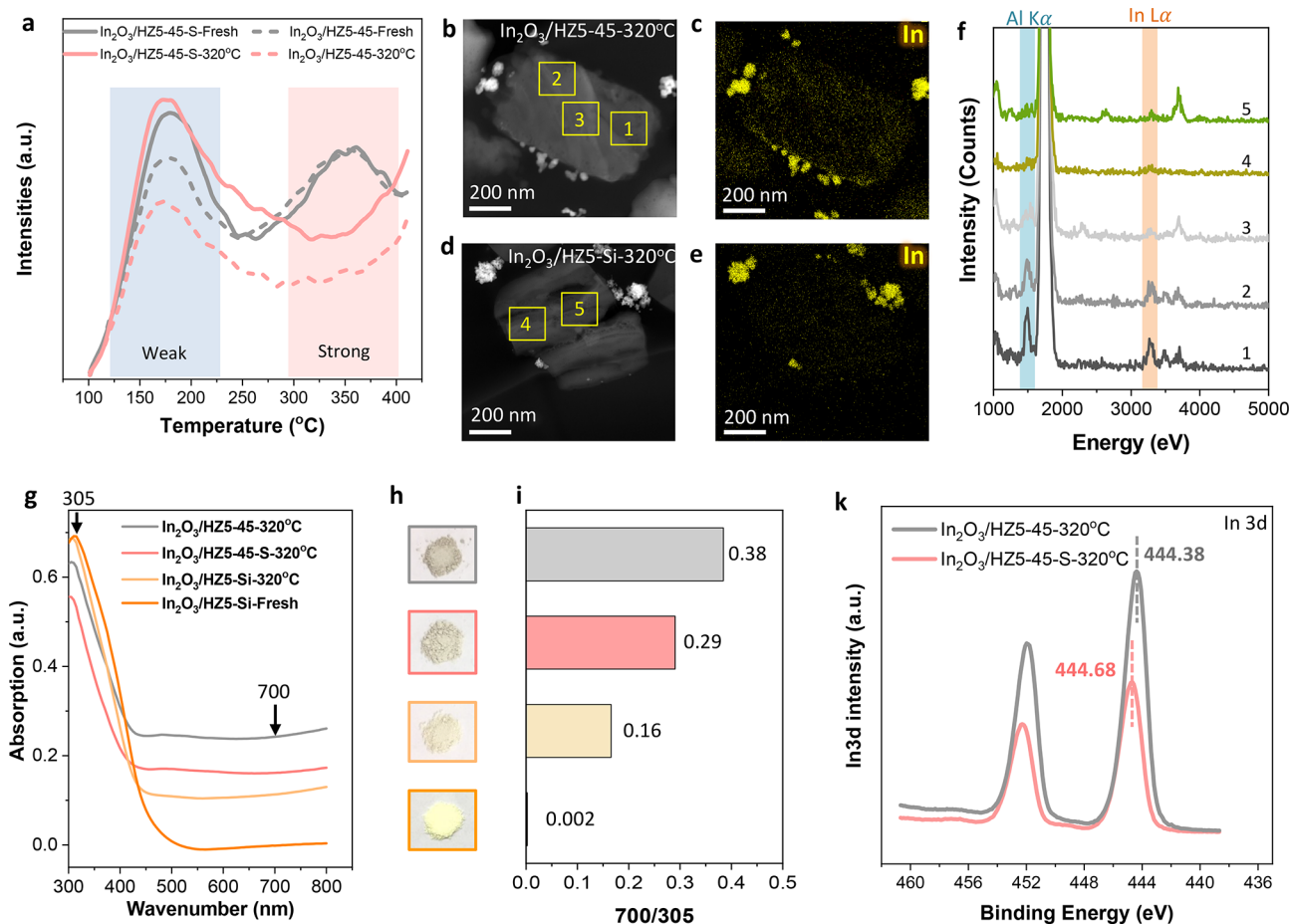
Figure 4. (a) Ammonia-temperature programmed desorption (NH$_3$-TPD) analysis of the fresh and used catalyst samples. According to the acidity results in Table 1 and to keep the tested acidity theoretically comparable for better comparison, the catalyst amount for the NH$_3$-TPD test was set as follows: 0.1457 g for both fresh and used In$_2$O$_3$/HZ5-45; 0.20 g for both fresh and used In$_2$O$_3$/HZ5-45-S. (b−e) High-angle annular dark-field−scanning transmission electron microscopy (HAADF−STEM) images (b,d) and energy-dispersive X-ray (EDX) spectroscopy mapping analysis (c,e) on the cross sections of the spent In$_2$O$_3$/HZ5-45 (b,c) and In$_2$O$_3$/HZ5-Si (d,e) catalyst materials under the same reaction conditions in Figure 3a. (f) EDX spectroscopy of typical areas in (b) and (d). (g) Ultraviolet−visible diffuse reflectance spectroscopy (UV−vis DRS) measurements with (h) corresponding optical images and (i) normalization of visible absorption by ultraviolet absorption (*i.e.*, the 700/305 nm band intensity ratio). (k) In 3d X-ray photoelectron spectroscopy (XPS) of the spent In$_2$O$_3$/HZ5-45 and In$_2$O$_3$/HZ5-45-S in Figure 3a.

material, the indium cations were supposed to be able to access the Al sites and neutralize the acid sites more readily. The corresponding catalytic performance showed no C$_2^+$ hydrocarbon formation as expected (Figure S12 and Table S1). All of these results suggested that the acid sites active for the MTH process within the HZ5-45 material were entirely neutralized by the migrated indium species.

Further analysis was performed to identify the type of indium species responsible for the deactivation. In$_2$O$_3$ was excluded as it was proven to be rather stable in the absence of hydrogen gas (see NH$_3$-TPD and Py-IR results in Figure S13a,b). Partially reduced In$_2$O$_3$ (Inδ^+, $0 < \delta < 3$) can be easily formed under a reducible atmosphere (see *in situ* Raman spectroscopy data and H$_2$-TPR characterization, Figure S14a,b). In particular, the formation of Inδ^+ was reported to increase the mobility of indium,[37] which accelerated the transfer to the acidic zeolite and resulted in its deactivation by neutralization. Thus, we propose that it was the formation and migration of the Inδ^+ species that caused the zeolite deactivation.

Surprisingly, indium was rarely found inside the silicalite-1 crystal (further denoted as HZ5-Si, Figure 4d,e). This result

demonstrates that the Inδ^+ species disliked migrating toward the Al-free zeolite, signifying the restraining role of this S-1 crystal on the migration of Inδ^+ species. Such a restraint probably explained the preservation of the acidity of the HZ5-45-S material (Figure 4a) that owned a nearly Al-free S-1 layer (Figure 2i and Table 1), which thus made the subsequent MTH conversion possible (Figure 3b). However, from the NH$_3$-TPD analysis (Figure 4a), after the reaction, a decent decrease was observed within the strong acid region, demonstrating that there could be still some indium contaminations on the S-1-coated material. The reason was possibly due to the presence of tiny amounts of Al within the shell (Figure 2i and Table 1) that acted as a bridge to allow a limited amount of Inδ^+ species to migrate into the HZ5-45-S material. However, this S-1-coated catalyst still showed quite good stability under the PM case (Figure S15).

Preventing Over-reduction of In$_2$O$_3$

The restrained migration of indium species by the S-1 layer in turn affected the properties of the In$_2$O$_3$ surface itself, as evidenced by the different optical colors of the In$_2$O$_3$/HZ5-45-PM and In$_2$O$_3$/HZ5-45-S-PM after the reaction (Figure 4h). This was confirmed by the distinct absorption in the

ultraviolet−visible diffuse reflectance spectroscopy (UV−vis DRS) data, shown in Figure 4g. The absorption in visible light (*e.g.*, 450−700 nm) was due to the formation of surface OVs by partial reduction.[51,52] Hess *et al.*, by using *operando* UV−vis spectroscopy, systematically elucidated the CO_2 hydrogenation process over In_2O_3 nanoparticles,[53] where the absorption at ∼700 nm was used to examine the oxygen defect change upon exposure to different gas phases or temperatures. However, from Figure 4g, the entire UV−vis DRS data did not shift upside along with the increase of visible-light absorbance, probably due to the presence of different zeolites. This could cause an inaccurate quantification of OVs solely by the absorbance at 700 nm. To better indicate the surface reduction level, we then used the absorption at 305 nm, which is the blueshift from the band gap at 330 nm of the bulk In_2O_3[54,55] to normalize the absorption intensity of visible light, taking 700 nm as an example, *i.e.*, the ratio of the 700/305 nm band intensity in Figure 4i. As identified in Figure S16a−g, a lower value of the 700/305 nm ratio meant a less severe reduction level of the In_2O_3 surface. Evidently from Figure 4i, the lower 700/305 nm value for the In_2O_3/HZ5-45-S material over In_2O_3/HZ5-45 (0.29 *vs* 0.38) demonstrated a lower reduction level of the In_2O_3 surface of the former catalyst.

According to the work by Müller *et al.*,[37] the over-reduction of In_2O_3 would lead to the formation of an amorphous phase on the surface or the appearance of metallic In^0, which caused the loss of activity. We then employed HRTEM to characterize the morphology of the In_2O_3 surface after the reaction. As shown in Figure S10c,f, the In_2O_3 surface/edge in the In_2O_3/HZ5-45-S was sharper compared to that in the In_2O_3/HZ5-45, signifying that In_2O_3 was less reduced in the S-1-coated catalyst. The valence of indium in the used catalyst was characterized by X-ray photoelectron spectroscopy (XPS). As shown in Figure 4k, a slightly higher binding energy of In 3d peaks of In_2O_3/HZ5-45-S over In_2O_3/HZ5-45 (for instance, 444.7 *vs* 444.4 eV) was observed, demonstrating that the In_2O_3 fraction in In_2O_3/HZ5-45-S was more oxidized than the latter one. All these results demonstrated that the In_2O_3 fraction in In_2O_3/HZ5-45-S was less reduced than that in In_2O_3/HZ5-45 after the reaction due to the presence of the S-1 shell. This prevented over-reduction of In_2O_3 by the S-1 shell that could be the result of the restrained migration of indium species as described above. Additionally, under the GM manner, the In_2O_3/HZ5-45-S showed almost doubled C_2^+ STY over the In_2O_3/HZ5-45 (Figure S9a), demonstrating that In_2O_3 was more active when coupled with the S-1-coated zeolite. In brief, this coated S-1 shell was deemed to be able to stabilize the In_2O_3 fraction, preventing it from being over-reduced during CO_2 hydrogenation.

Suppressing Zeolite Coking

Apart from the deactivation by the $In\delta^+$ species, the zeolites also suffered from coking when working on the MTH conversion, which is the second stage of the methanol-mediated CO_2 hydrogenation.[18,27,29] In MTH chemistry, the selective formation of hydrocarbons within a zeolite is believed to be the synergy of the olefinic and aromatic cycles. The coke, especially the exterior coke deposits, is the main reason for zeolite deactivation.[56,57] Exterior coke, referring to the polyaromatics outside of the zeolite crystals that block the pore channel, is formed by the secondary reaction of charged aromatics, the major products from the aromatic cycle. Different strategies, *i.e.*, isolating the Brønsted acid site to

inhibit secondary reactions[58] or regulating the zeolite surface morphology[59] or permeability,[60] have been proposed to prevent the exterior coke formation in MTH chemistry.

Here, coating such an S-1 layer also showed promising capacity in preventing exterior coking. Due to a rather low methanol flux from the CTM, coking in this bifunctional system is usually low over the course of a limited time period.[18,27] We then accelerated the coking process by introducing a much higher methanol flux (*ca.* 100 mmol/$g_{zeolite}$/h) compared to the CTM process (equivalent max. 2.6 mmol/$g_{zeolite}$/h, Figure S9d). Considering the similar Al sittings of these two zeolites (Table S2 and Figure S17), we added inactive SiO_2 (synthesis details can be found in the Supporting Information) to the pristine HZ5-45 with a mass ratio of 1.2 (denoted as HZ5-45-SiO_2, Figure S18) to keep a comparable acidity to that of HZ5-45-S. MTH test results from Figure 5a,b showed that HZ5-45-S held a longer MTH lifetime by *ca.* 36% increase (30.h *vs* 22.h) compared to that of HZ5-45-SiO_2, demonstrating the better coke resistance by the presence of an S-1 shell.
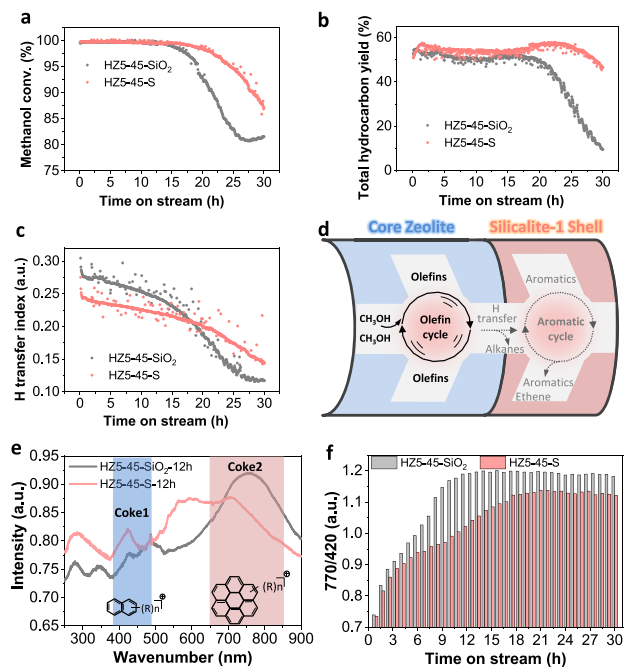

Figure 5. (a−c) Methanol-to-hydrocarbon (MTH) performance of (a) methanol conversion, (b) total hydrocarbon yield excluding dimethylether (DME), and (c) hydrogen transfer index (HTI) of catalyst HZ5-45-SiO_2 and HZ5-45-S as a functional of methanol stream time. Zeolite HZ5-45 was deactivating quickly after 22 h as the hydrocarbon yield decreased sharply even with a decent methanol conversion. HTI was calculated as the ratio of the selectivity of C_1−C_5 alkanes to the selectivity of C_1−C_5 alkanes and C_2−C_4 olefins. (d) Illustration of the shell effect on the MTH mechanism, *i.e.*, preventing the aromatic cycle in the dual cycle mechanism. The dashed lines mean the suppressed pathways. MTH reaction conditions: methanol weight hourly space velocity (WSHV) = 3.2 h^{-1}, T = 360 °C. (e) Comparison of the *operando* UV−vis diffuse reflectance spectroscopy (DRS) data collected at 12 h of MTH with the difference in the absorption intensity of coke 1 (e.g., charged benzenes) and coke 2 (e.g., charged polyaromatics) marked in the blue and red region. (f) Intensity normalization of the 770 nm absorption band by the 420 nm absorption band as a function of time-on-stream.

This S-1-induced suppression of zeolite coking could be attributed to the altered behaviors of the olefinic and aromatic cycles, operative in the MTH process. The hydrogen transfer index (HTI), calculated as the ratio of alkanes to (alkanes + alkenes), is considered to be a good indicator to elucidate the relationships between these two cycles.[61] A lower HTI value means less hydrogen transfer and a less dominant aromatic cycle and therefore also less coke formation. The lower HTI value of HZ5-45-S in the first 20 h (Figure 5c) compared to HZ5-45-SiO$_2$ suggested less hydrogen transferring within the S-1-coated zeolites during MTH and hence a reduced contribution of the aromatic cycle to the MTH process. This can be corroborated by the decreased selectivity of the typical aromatic cycle products of HZ5-45-S, *i.e.*, the lower ethylene and aromatic selectivity, compared to that of HZ5-45-SiO$_2$ (Figure S19d,e). The measurements of *operando* UV−vis DRS measurements (Figure 5e and Figure S20) further validated this result. The absorption at a high wavenumber (*e.g.*, 770 nm) referred to the formation of exterior coke species of the polycondensed aromatics.[62,63] The lower absorption intensity at 770 nm for HZ5-45-S after 12 h of MTH demonstrated that there was less exterior coke formation compared to HZ5-45-SiO$_2$. The intensity normalization of the absorption at 700 nm by the absorption at 420 nm (*i.e.*, the interior coke species) was considered to better illustrate the coking behavior,[57] thereby further signifying the lower level of exterior coking of HZ5-45-S within the whole MTH period (Figure 5f). All of these results demonstrated that the aromatic cycle was suppressed due to the introduction of the coated S-1 layer (as illustrated in Figure 5d), which thereby prevented the formation of exterior coke and resulted in a prolonged MTH lifetime. With reference to the CO$_2$ hydrogenation system, after the reaction, the S-1-coated catalyst also showed a smaller amount of coke deposits and a lower absorption intensity compared to the pristine one, as indicated by the thermogravimetric analysis-mass spectroscopy (TGA-MS) data, shown in Figure S21a,b, and the UV−vis DRS data, shown in Figure S21c. This was also corroborated by the lighter optical color of the used In$_2$O$_3$/HZ5-45-S (Figure S21d). All of these results therefore demonstrated that the coated S-1 shell formed around the zeolite ZSM-5 crystal was able to slow down the coking formation process during catalytic CO$_2$ hydrogenation.

CONCLUSIONS

We have demonstrated that coating an acidic zeolite with an S-1 shell resulted in multiple benefits in securing the bifunctional nature of the In$_2$O$_3$/zeolite catalyst material for carbon chain propagations from CO$_2$ hydrogenation. First, the S-1 coating can prevent the contamination of indium cations on the zeolite material, by which the carbon chain propagations inside the zeolite channel system were successfully retrieved under nanoscale proximity. Due to the prohibited migration of indium species, the surface of In$_2$O$_3$ was in turn well-stabilized instead of over-reduced, through which a higher CO$_2$ hydrogenation performance including an improved CO$_2$ conversion and C$_2$$^+$ hydrocarbon yield was achieved. Additionally, the introduction of the S-1 shell was able to prolong the lifetime of zeolite when tackling the methanol-mediated bifunctional catalysis approach due to the prohibited aromatic cycle. This work highlighted a promising "shielding strategy" to secure the bifunctional catalytic chemistry during CO$_2$ thermocatalysis.

EXPERIMENTAL SECTION

Synthesis of Catalytic Materials

Synthesis of Zeolite H-ZSM-5. Zeolite H-ZSM-5 with a Si/Al ratio of 45 was synthesized according to the work of the group of Rimer with some slight modification.[62] Typically, 2.86 g of tetra-*n*-propylammonium hydroxide (TPAOH, 20 w%, Alfa Aesar) was added into 10.26 g of distilled water inside a 50 mL centrifuge tube. Then, a solution of 0.30 g of 10 wt % NaOH was dropped inside. After that, 0.035 g of sodium aluminate (technical grade, Alfa Aesar) was dissolved under soft stirring until fully dissolved. Thereafter, 4 g of tetraethylorthosilicate (TEOS, 99%, Sigma-Aldrich) was dropped inside followed by stirring at 1000 rpm at room temperature for 5 h to obtain a transparent synthesis liquid. The molar ratio of TEOS:Al:TPAOH:H$_2$O:NaOH was 1:0.022:0.15:37:0.04. Then, the liquid was transferred into a 25 mL autoclave with a teflon liner. After 3 days of rotation under 170 °C, the autoclave was taken out and quenched by tap water. The solid product was achieved after washing with distilled water and centrifugation at 5000 rpm three times. After drying at 100 °C overnight, zeolite ZSM-5 powder was obtained after calcination at 550 °C for 8 h with a ramping rate of 1 °C/min to remove the organic template TPAOH. An ion exchange with 1 M ammonium nitrate solution at 70 °C for 6 h was used to remove sodium ions inside zeolite channels. After drying at 100 °C followed by the same calcination described above, the H-ZSM-5 was finally obtained (denoted as HZ5-45). The synthesis of HZ5-105 followed the same procedure of HZ5-45 with a different sodium aluminate amount (0.015 g). The synthesis of HZ5-Si also followed the same procedure of HZ5-45 without the addition of sodium aluminate.

Synthesis of HZ5-45-S by Secondary Growth. A mother liquid was prepared with mixing 1.54 g of TPAOH, 12.64 g of distilled water, 2.4 g of ethanol, and 2.5 g of TEOS into a 50 mL centrifuge tube. The liquid mixture was then stirred at room temperature for 5 h until all TEOS was hydrolyzed. Then, 0.5 g of HZ5-45 as the core zeolite was added into the tube and sonicated for 10 min to achieve a full dispersion of zeolite crystals. After that, the tube was sealed and laid in a 95 °C oil bath for 24 h with a stirring rate of 500 rpm for the secondary growth. Thereafter, the solid product was achieved after washing with distilled water and centrifugation at 5000 rpm three times. After drying at 100 °C overnight, zeolite HZ5-45 coated with a shell (denoted as HZ5-45-S) powder was obtained after calcination at 550 °C for 8 h with a ramping rate of 1 °C/min to remove the organic template TPAOH. The synthesis of zeolite CBV8014-S coated with an S-1 shell followed the same procedure as that of HZ5-45-S using CBV8014 (Zeolyst) as the core zeolite.

Synthesis of other materials including In$_2$O$_3$, HZ5-45-SiO$_2$, and the In$_2$O$_3$/zeolite bifunctional catalysts with different mixing manners can be found in the experimental details in the Supporting Information.

Catalyst Characterization

X-ray diffraction (XRD) was performed on a Bruker-AXS D2 Phaser X-ray diffractometer in the Bragg−Brentano mode, equipped with a Lynxeye detector (Co Kα, λ = 1.790 Å). Argon physisorption was conducted using a Micromeritics Tristar 3000 surface area analyzer operating at −196 °C. The morphologies of In$_2$O$_3$ and H-ZSM-5 were visualized by a scanning electronic microscope (SEM, XL30). Ammonia-temperature programmed desorption (NH$_3$-TPD) on a Micromeritics AutoChemII 2920 instrument equipped with a thermal conductivity detector (TCD) was used to indicate the total acid amounts. The catalyst amount for the NH$_3$-TPD test was set as follows: 0.1 g for HZ5-45, HZ5-45-S, and HZ5-105, 0.1457 g for fresh and used In$_2$O$_3$/HZ5-45, and 0.20 g for fresh and used In$_2$O$_3$/HZ5-45-S. The weak acidity referred to the desorption peak at the range of 125−250 °C, while the strong acidity corresponded to that of 275−400 °C. The specific amount of weak and strong acid sites was acquired by the Gaussian fitting over the raw NH$_3$-TPD curve. The Brønsted and Lewis acid ratio (B/L) was achieved by pyridine infrared spectroscopy (Py-IR) using a Nicolet iZ10-IR spectrometer. High-angle annular dark-field−scanning transmission electron microscopy (HAADF−STEM) imaging and energy-dispersive X-ray

spectroscopy (EDX) line scanning and mapping were performed on a Talos F200X (FEI) microscope at 200 keV, which is equipped with an X-FEG electron source and a Super-X detector. Before the analysis, ultramicrotomy of resin-embedded catalysts was carried out. A tiny amount of the catalyst was first embedded in Epofix resin and then put in room temperature overnight until it became a solid and was cut to 150 nm sections using a diamond knife. Sections were then deposited on carbon-coated copper TEM grids (200 mesh). The surface Al and Si elemental distribution of catalysts was determined by X-ray photoelectron spectroscopy on a PHI 5000 Versaprobe scanning ESCA microprobe (Physical Electronics) with a mono-chromatized Al Kα X-ray source (beam diameter of 200 μm, X-ray power of 50 W). Surface In and O elements of catalysts were measured by another XPS setup (Thermo Scientific ESCALAB 250 Xi). The binding energies were calibrated by setting the C 1s adventitious carbon peak position to 284.8 eV. *In situ* Raman spectroscopy measurements on In_2O_3 were performed using a Renishaw inVia microscope coupled with a FTIR600 Linkam reactor. The Al pairs in zeolites were characterized by ultraviolet−visible diffuse reflectance spectroscopy (UV−vis DRS) using a PerkinElmer Lambda 940 spectrophotometer equipped with an integrating "Labsphere", where a pure white polytetrafluoroethylene was used as a white background. Prior to the UV−vis DRS measurement, the Co(II) ion-exchanged zeolites were first dehydrated at 250 °C under vacuum conditions and then transferred to a glovebox to avoid being exposed to air and loaded into a sealed UV−vis cell. The adsorption intensity was obtained by the calculation using the Schuster−Kubelka−Munk equation $F(R_\infty) = (1 - R_\infty)^2/2R_\infty$. The elemental (Si, Al, Na, and Co) ratios in bulk zeolite crystals were identified by the inductively coupled plasma−optical emission spectroscopy (ICP-OES) measurements using a Spectro Arcos instrument.

Catalytic Testing

The CO_2 hydrogenation reaction was conducted using a home-made fixed-bed reactor connected with an online GC (Interscience modified Thermo Fischer Scientific TraceGC 1300) equipped with a column (Restek RTX-502.2, 60 m × 0.32 mm ID). A diameter of 12 mm stainless steel tube with the inner wall coated by a thin layer of quartz constituted the main part for catalysis reaction. A typical procedure for testing was as follows: 1 g of catalyst was loaded inside the tube by quartz wool and held by a thin quartz tube. After leak checking, the catalyst was first calcined under argon flow (10 mL/min) at 320 °C for 2 h with a ramping rate of 5 °C/min and then cooled down to 50 °C. After that, the gas channel was switched to CO_2, H_2, and Ar with a volume ratio of 6:18:1. Argon was added as an internal standard. When the reactor reached 20 bars as being set ahead, gas was kept flowing for 3 h until the outlet gas composition was stable. Then, the reaction started by ramping the reactor at 5 °C/min to the desired temperature (*e.g.*, 300, 320, 340, and 360 °C). The data were collected after five hours of reaction running. For the granule mixing test, In_2O_3 and zeolite were first pressed, crushed and sieved to a 40−60 mesh, and then physically mixed. For the powder mixing test, In_2O_3 and zeolite powders were first ground in a mortar and then pressed, crushed, and sieved to the same mesh.

Detailed calculations were performed for the evaluation of catalyst performance.

The yield of converted CO_2 (in flow rate, mL/min) was calculated as follows:

$$\text{reacted } CO_2 = F_{CO_2} - F_{Ar} \times \frac{A_{CO_2}}{A_{Ar}} \times f_{CO_2/Ar}$$

where F_{CO_2} and F_{Ar} are the CO_2 and Ar inlet volume flow rates, A_{Ar} and A_{CO_2} are the TCD peak areas of Ar and CO_2 during the reaction, and $f_{CO_2/Ar}$ is the relative calibration factor (CO_2 vs Ar, 0.4481).

The CO_2 conversion was calculated as follows:

CO_2 conversion (%)

$$= \frac{\text{reacted } CO_2}{F_{CO_2}}$$

$$= \left(1 - \frac{F_{Ar} \times A_{CO_2}}{F_{CO_2} \times A_{Ar}} \times f_{CO_2/Ar}\right) \times 100\%$$

The CO yield (in flow rate, mL/min) was calculated as follows:

$$\text{CO yield} = \frac{F_{Ar} \times A_{CO}}{A_{Ar}} \times f_{CO/Ar}$$

where A_{CO} is the TCD peak area of produced CO during the reaction and $f_{CO/Ar}$ is the relative calibration factor (CO vs Ar, 1.04).

The CO selectivity was calculated as follows:

$$S_{CO} (\%) = \frac{\text{CO yield}}{\text{reacted } CO_2} \times 100\%$$

The selectivity toward hydrocarbons or organic oxygenate products was calculated as follows:

$$S_i(\%) = \frac{A_i \times f_i}{\sum_{i=1}^{\max} A_i \times f_i} \times 100\%$$

where A_i and f_i are the FID peak area and the calibration factor of product i, respectively.

The C_2^+ selectivity on carbon basis was calculated as follows:

$$S_{C_2^+}(\%) = 100\% - S_{CO} - S_{CH_4} - S_{methanol} - S_{DME}$$

The space−time yield (STY) of C_2^+ was calculated as follows:

$$STY_{C_2^+} = STY_{\text{reacted } CO_2} - STY_{CO} - STY_{CH_4} - STY_{methanol} - STY_{DME}$$

$$STY_{\text{reacted } CO_2} = \frac{\text{reacted } CO_2 \times 60}{22.4 \times m_{oxides}} \times \frac{273}{423}$$

$$STY_{CO} = \frac{\text{CO yield} \times 60}{22.4 \times m_{oxides}} \times \frac{273}{423}$$

$$STY_{CH_4} = (STY_{\text{reacted } CO_2} - STY_{CO}) \times S_{CH_4}$$

$$STY_{methanol} = (STY_{\text{reacted } CO_2} - STY_{CO}) \times S_{methanol}$$

$$STY_{DME} = (STY_{\text{reacted } CO_2} - STY_{CO}) \times S_{DME}$$

The methanol-to-hydrocarbon (MTH) conversion was performed in a quartz, rectangular fixed-bed reactor (ID 6 mm × 3 mm). The MTH reaction at high pressure highly prolonged the lifetime of zeolite, but the product selectivity was not much pressure-sensitive.[64] Herein, we have performed the MTH reaction under the ambient pressure to investigate the performance of these three zeolites at a reaction temperature of 360 °C that was comparable with investigated CO_2 hydrogenation. In all experiments, 160 mg of zeolite was used, with a particle size of 0.2−0.4 mm. The methanol flow was achieved by flowing He as the carrier gas through a methanol saturator where the methanol saturation was *ca.* 14% at 22 °C. The weight hourly space velocity (WHSV) was 3.2 h^{-1}, that is, *ca.* 100 mmol of methanol/g$_{zeolite}$/h. *Operando* UV−vis DRS spectra were recorded using an AvaSpec 2048L spectrometer *via* a high-temperature UV−vis optical fiber probe. Online analysis of the reactant and MTH products was realized by an Interscience Compact GC, equipped with Rtx-wax and Rtx-1 columns in series and Rtx-1, Rt-TCEP, and Al_2O_3/Na_2SO_4 columns in series, both of them connected to an FID detector. We set the methanol conversion of 85% as the end of the experiment.

The methanol conversion was calculated as follows:

methanol conversion (%)

$$= \frac{[\text{methanol}_{\text{in}}] - [\text{methanol}_{\text{out}}]}{[\text{methanol}_{\text{in}}]} \times 100\%$$

The selectivity of MTH product i was calculated based on the carbon basis as follows:

$$S_{C_iH_j} = \frac{i \times [C_iH_j]}{[\text{methanol}_{\text{in}}] - [\text{methanol}_{\text{out}}]} \times 100\%$$

The hydrogen transfer index (HTI) was calculated as the ratio of alkanes to (alkanes + alkenes) as follows:

$$\text{HTI} = \frac{\sum_1^5 S_{C_i^0}}{\sum_1^5 S_{C_i^0} + \sum_2^5 S_{C_i^=}}$$

$S_{C_i^0}$ and $S_{C_i^=}$ represent the selectivity of alkane and alkene of i.

■ ASSOCIATED CONTENT

Ⓢ Supporting Information

The Supporting Information is available free of charge at https://pubs.acs.org/doi/10.1021/jacsau.2c00621.

> Details of synthesis of additional catalysts; catalyst characterization results including TEM, Py-IR, NH$_3$-TPD, Ar physisorption, Raman spectroscopy, H$_2$-TPR, XPS, UV−vis, Co(II) UV−vis DRS, TG-MS, *etc.*; CO$_2$ hydrogenation performance; comparison with literature work; catalytic performance and *operando* UV−vis spectra of MTH conversion catalyzed by different zeolites (PDF)

■ AUTHOR INFORMATION

Corresponding Author

Bert M. Weckhuysen − *Inorganic Chemistry and Catalysis Group, Debye Institute for Nanomaterial Science and Institute for Sustainable and Circular Chemistry, Utrecht University, 3584 CG Utrecht, The Netherlands;* ⓞ orcid.org/0000-0001-5245-1426; Email: B.M.Weckhuysen@uu.nl

Authors

Shiyou Xing − *Inorganic Chemistry and Catalysis Group, Debye Institute for Nanomaterial Science and Institute for Sustainable and Circular Chemistry, Utrecht University, 3584 CG Utrecht, The Netherlands; Guangzhou Institute of Energy Conversion, Chinese Academy of Sciences, CAS Key Laboratory of Renewable Energy, Guangdong Provincial Key Laboratory of New and Renewable Energy Research and Development, Guangzhou 510640 Guangdong Province, China*

Savannah Turner − *Materials Chemistry and Catalysis Group, Debye Institute for Nanomaterial Science, Utrecht University, 3584 CG Utrecht, The Netherlands*

Donglong Fu − *Inorganic Chemistry and Catalysis Group, Debye Institute for Nanomaterial Science and Institute for Sustainable and Circular Chemistry, Utrecht University, 3584 CG Utrecht, The Netherlands*

Sophie van Vreeswijk − *Inorganic Chemistry and Catalysis Group, Debye Institute for Nanomaterial Science and Institute for Sustainable and Circular Chemistry, Utrecht University, 3584 CG Utrecht, The Netherlands*

Yuanshuai Liu − *Inorganic Chemistry and Catalysis Group, Debye Institute for Nanomaterial Science and Institute for Sustainable and Circular Chemistry, Utrecht University, 3584 CG Utrecht, The Netherlands;* ⓞ orcid.org/0000-0002-4020-7538

Jiadong Xiao − *Inorganic Chemistry and Catalysis Group, Debye Institute for Nanomaterial Science and Institute for Sustainable and Circular Chemistry, Utrecht University, 3584 CG Utrecht, The Netherlands;* ⓞ orcid.org/0000-0001-9130-5376

Ramon Oord − *Inorganic Chemistry and Catalysis Group, Debye Institute for Nanomaterial Science and Institute for Sustainable and Circular Chemistry, Utrecht University, 3584 CG Utrecht, The Netherlands*

Joachim Sann − *Institute of Physical Chemistry, Center for Materials Research (LaMa), Justus-Liebig-University, 35392 Gießen, Germany*

Complete contact information is available at: https://pubs.acs.org/10.1021/jacsau.2c00621

Author Contributions

All authors have approved the final version of the manuscript.

Notes

The authors declare no competing financial interest.

■ ACKNOWLEDGMENTS

■ REFERENCES

(1) Álvarez, A.; Bansode, A.; Urakawa, A.; Bavykina, A. V.; Wezendonk, T. A.; Makkee, M.; Gascon, J.; Kapteijn, F. Challenges in the Greener Production of Formates/Formic Acid, Methanol, and DME by Heterogeneously Catalyzed CO$_2$ Hydrogenation Processes. *Chem. Rev.* **2017**, *117*, 9804−9838.

(2) Zhong, J.; Yang, X.; Wu, Z.; Liang, B.; Huang, Y.; Zhang, T. State of the art and perspectives in heterogeneous catalysis of CO$_2$ hydrogenation to methanol. *Chem. Soc. Rev.* **2020**, *49*, 1385−1413.

(3) Zhou, W.; Cheng, K.; Kang, J.; Zhou, C.; Subramanian, V.; Zhang, Q.; Wang, Y. New horizon in C1 chemistry: breaking the selectivity limitation in transformation of syngas and hydrogenation of CO$_2$ into hydrocarbon chemicals and fuels. *Chem. Soc. Rev.* **2019**, *48*, 3193−3228.

(4) Rodriguez, J. A.; Evans, J.; Feria, L.; Vidal, A. B.; Liu, P.; Nakamura, K.; Illas, F. CO$_2$ hydrogenation on Au/TiC, Cu/TiC, and Ni/TiC catalysts: Production of CO, methanol, and methane. *J. Catal.* **2013**, *307*, 162−169.

(5) Ye, J.; Ge, Q.; Liu, C.-j. Effect of PdIn bimetallic particle formation on CO$_2$ reduction over the Pd−In/SiO$_2$ catalyst. *Chem. Eng. Sci.* **2015**, *135*, 193−201.

(6) Wang, C.; Guan, E.; Wang, L.; Chu, X.; Wu, Z.; Zhang, J.; Yang, Z.; Jiang, Y.; Zhang, L.; Meng, X.; Gates, B. C.; Xiao, F.-S. Product Selectivity Controlled by Nanoporous Environments in Zeolite Crystals Enveloping Rhodium Nanoparticle Catalysts for CO$_2$ Hydrogenation. *J. Am. Chem. Soc.* **2019**, *141*, 8482−8488.

(7) Vogt, C.; Groeneveld, E.; Kamsma, G.; Nachtegaal, M.; Lu, L.; Kiely, C. J.; Berben, P. H.; Meirer, F.; Weckhuysen, B. M. Unravelling

structure sensitivity in CO_2 hydrogenation over nickel. *Nat. Catal.* **2018**, *1*, 127−134.

(8) Vogt, C.; Monai, M.; Kramer, G. J.; Weckhuysen, B. M. The renaissance of the Sabatier reaction and its applications on Earth and in space. *Nat. Catal.* **2019**, *2*, 188−197.

(9) Schaub, T.; Paciello, R. A. A Process for the Synthesis of Formic Acid by CO_2 Hydrogenation: Thermodynamic Aspects and the Role of CO. *Angew. Chem., Int. Ed.* **2011**, *50*, 7278−7282.

(10) Liu, Q.; Yang, X.; Li, L.; Miao, S.; Li, Y.; Li, Y.; Wang, X.; Huang, Y.; Zhang, T. Direct catalytic hydrogenation of CO_2 to formate over a Schiff-base-mediated gold nanocatalyst. *Nat. Commun.* **2017**, *8*, 1407.

(11) Kattel, S.; Ramírez, P. J.; Chen, J. G.; Rodriguez, J. A.; Liu, P. Active sites for CO_2 hydrogenation to methanol on Cu/ZnO catalysts. *Science* **2017**, *355*, 1296−1299.

(12) Wang, J.; Li, G.; Li, Z.; Tang, C.; Feng, Z.; An, H.; Liu, H.; Liu, T.; Li, C. A highly selective and stable ZnO-ZrO$_2$ solid solution catalyst for CO_2 hydrogenation to methanol. *Sci. Adv.* **2017**, *3*, e1701290.

(13) Lam, E.; Larmier, K.; Wolf, P.; Tada, S.; Safonova, O. V.; Coperet, C. Isolated Zr Surface Sites on Silica Promote Hydrogenation of CO_2 to CH_3OH in Supported Cu Catalysts. *J. Am. Chem. Soc.* **2018**, *140*, 10530−10535.

(14) Gao, P.; Dang, S.; Li, S.; Bu, X.; Liu, Z.; Qiu, M.; Yang, C.; Wang, H.; Zhong, L.; Han, Y.; Liu, Q.; Wei, W.; Sun, Y. Direct Production of Lower Olefins from CO_2 Conversion via Bifunctional Catalysis. *ACS Catal.* **2018**, *8*, 571−578.

(15) Ma, Z.; Porosoff, M. D. Development of Tandem Catalysts for CO_2 Hydrogenation to Olefins. *ACS Catal.* **2019**, *9*, 2639−2656.

(16) Ni, Y.; Chen, Z.; Fu, Y.; Liu, Y.; Zhu, W.; Liu, Z. Selective conversion of CO_2 and H_2 into aromatics. *Nat. Commun.* **2018**, *9*, 3457.

(17) Wang, Y.; Tan, L.; Tan, M.; Zhang, P.; Fang, Y.; Yoneyama, Y.; Yang, G.; Tsubaki, N. Rationally Designing Bifunctional Catalysts as an Efficient Strategy To Boost CO_2 Hydrogenation Producing Value-Added Aromatics. *ACS Catal.* **2019**, *9*, 895−901.

(18) Gao, P.; Li, S.; Bu, X.; Dang, S.; Liu, Z.; Wang, H.; Zhong, L.; Qiu, M.; Yang, C.; Cai, J.; Wei, W.; Sun, Y. Direct conversion of CO_2 into liquid fuels with high selectivity over a bifunctional catalyst. *Nat. Chem.* **2017**, *9*, 1019.

(19) Wei, J.; Ge, Q.; Yao, R.; Wen, Z.; Fang, C.; Guo, L.; Xu, H.; Sun, J. Directly converting CO_2 into a gasoline fuel. *Nat. Commun.* **2017**, *8*, 15174.

(20) Ramirez, A.; Sarathy, S. M.; Gascon, J. CO_2 Derived E-Fuels: Research Trends, Misconceptions, and Future Directions. *Trends Chem.* **2020**, *2*, 785−795.

(21) Aitbekova, A.; Goodman, E. D.; Wu, L.; Boubnov, A.; Hoffman, A. S.; Genc, A.; Cheng, H.; Casalena, L.; Bare, S. R.; Cargnello, M. Engineering of Ruthenium−Iron Oxide Colloidal Heterostructures: Improved Yields in CO_2 Hydrogenation to Hydrocarbons. *Angew. Chem., Int. Ed.* **2019**, *58*, 17451−17457.

(22) Liu, X.; Wang, M.; Zhou, C.; Zhou, W.; Cheng, K.; Kang, J.; Zhang, Q.; Deng, W.; Wang, Y. Selective transformation of carbon dioxide into lower olefins with a bifunctional catalyst composed of ZnGa$_2$O$_4$ and SAPO-34. *Chem. Commun.* **2018**, *54*, 140−143.

(23) Jiao, F.; Li, J.; Pan, X.; Xiao, J.; Li, H.; Ma, H.; Wei, M.; Pan, Y.; Zhou, Z.; Li, M.; Miao, S.; Li, J.; Zhu, Y.; Xiao, D.; He, T.; Yang, J.; Qi, F.; Fu, Q.; Bao, X. Selective conversion of syngas to light olefins. *Science* **2016**, *351*, 1065−1068.

(24) Li, Y.; Wang, M.; Liu, S.; Wu, F.; Zhang, Q.; Zhang, S.; Cheng, K.; Wang, Y. Distance for Communication between Metal and Acid Sites for Syngas Conversion. *ACS Catal.* **2022**, *12*, 8793−8801.

(25) Cheng, K.; Smulders, L. C. J.; van der Wal, L. I.; Oenema, J.; Meeldijk, J. D.; Visser, N. L.; Sunley, G.; Roberts, T.; Xu, Z.; Doskocil, E.; Yoshida, H.; Zheng, Y.; Zečević, J.; de Jongh, P. E.; de Jong, K. P. Maximizing noble metal utilization in solid catalysts by control of nanoparticle location. *Science* **2022**, *377*, 204−208.

(26) Fujiwara, M.; Satake, T.; Shiokawa, K.; Sakurai, H. CO_2 hydrogenation for C_2^+ hydrocarbon synthesis over composite catalyst using surface modified HB zeolite. *Appl. Catal. B* **2015**, *179*, 37−43.

(27) Li, Z.; Qu, Y.; Wang, J.; Liu, H.; Li, M.; Miao, S.; Li, C. Highly Selective Conversion of Carbon Dioxide to Aromatics over Tandem Catalysts. *Joule* **2019**, *3*, 570−583.

(28) Zhou, C.; Shi, J.; Zhou, W.; Cheng, K.; Zhang, Q.; Kang, J.; Wang, Y. Highly Active ZnO-ZrO$_2$ Aerogels Integrated with H-ZSM-5 for Aromatics Synthesis from Carbon Dioxide. *ACS Catal.* **2020**, *10*, 302−310.

(29) Numpilai, T.; Wattanakit, C.; Chareonpanich, M.; Limtrakul, J.; Witoon, T. Optimization of synthesis condition for CO_2 hydrogenation to light olefins over In$_2$O$_3$ admixed with SAPO-34. *Energy Convers. Manage.* **2019**, *180*, 511−523.

(30) Martin, O.; Martín, A. J.; Mondelli, C.; Mitchell, S.; Segawa, T. F.; Hauert, R.; Drouilly, C.; Curulla-Ferré, D.; Pérez-Ramírez, J. Indium Oxide as a Superior Catalyst for Methanol Synthesis by CO_2 Hydrogenation. *Angew. Chem., Int. Ed.* **2016**, *55*, 6261−6265.

(31) Dang, S.; Li, S.; Yang, C.; Chen, X.; Li, X.; Zhong, L.; Gao, P.; Sun, Y. Selective Transformation of CO_2 and H_2 into Lower Olefins over In$_2$O$_3$-ZnZrOx/SAPO-34 Bifunctional Catalysts. *ChemSusChem* **2019**, *12*, 3582−3591.

(32) Wang, S.; Wang, P.; Qin, Z.; Yan, W.; Dong, M.; Li, J.; Wang, J.; Fan, W. Enhancement of light olefin production in CO_2 hydrogenation over In$_2$O$_3$-based oxide and SAPO-34 composite. *J. Catal.* **2020**, *391*, 459−470.

(33) Cheng, K.; Zhou, W.; Kang, J.; He, S.; Shi, S.; Zhang, Q.; Pan, Y.; Wen, W.; Wang, Y. Bifunctional Catalysts for One-Step Conversion of Syngas into Aromatics with Excellent Selectivity and Stability. *Chem* **2017**, *3*, 334−347.

(34) Cheng, K.; Gu, B.; Liu, X.; Kang, J.; Zhang, Q.; Wang, Y. Direct and Highly Selective Conversion of Synthesis Gas into Lower Olefins: Design of a Bifunctional Catalyst Combining Methanol Synthesis and Carbon−Carbon Coupling. *Angew. Chem., Int. Ed.* **2016**, *55*, 4725−4728.

(35) Zecevic, J.; Vanbutsele, G.; de Jong, K. P.; Martens, J. A. Nanoscale intimacy in bifunctional catalysts for selective conversion of hydrocarbons. *Nature* **2015**, *528*, 245−248.

(36) Wang, Y.; Wang, G.; van der Wal, L. I.; Cheng, K.; Zhang, Q.; de Jong, K. P.; Wang, Y. Visualizing Element Migration over Bifunctional Metal-Zeolite Catalysts and its Impact on Catalysis. *Angew. Chem., Int. Ed.* **2021**, *60*, 17735−17743.

(37) Tsoukalou, A.; Abdala, P. M.; Stoian, D.; Huang, X.; Willinger, M.-G.; Fedorov, A.; Müller, C. R. Structural Evolution and Dynamics of an In$_2$O$_3$ Catalyst for CO_2 Hydrogenation to Methanol: An Operando XAS-XRD and In Situ TEM Study. *J. Am. Chem. Soc.* **2019**, *141*, 13497−13505.

(38) Li, W.; Wang, K.; Zhan, G.; Huang, J.; Li, Q. Design and Synthesis of Bioinspired ZnZrOx&Bio-ZSM-5 Integrated Nanocatalysts to Boost CO_2 Hydrogenation to Light Olefins. *ACS Sustainable Chem. Eng.* **2021**, *9*, 6446−6458.

(39) Masoumifard, N.; Guillet-Nicolas, R.; Kleitz, F. Synthesis of Engineered Zeolitic Materials: From Classical Zeolites to Hierarchical Core−Shell Materials. *Adv. Mater.* **2018**, *30*, 1704439.

(40) Das, S.; Pérez-Ramírez, J.; Gong, J.; Dewangan, N.; Hidajat, K.; Gates, B. C.; Kawi, S. Core−shell structured catalysts for thermocatalytic, photocatalytic, and electrocatalytic conversion of CO_2. *Chem. Soc. Rev.* **2020**, *49*, 2937−3004.

(41) Přech, J.; Strossi Pedrolo, D. R.; Marcilio, N. R.; Gu, B.; Peregudova, A. S.; Mazur, M.; Ordomsky, V. V.; Valtchev, V.; Khodakov, A. Y. Core−Shell Metal Zeolite Composite Catalysts for In Situ Processing of Fischer−Tropsch Hydrocarbons to Gasoline Type Fuels. *ACS Catal.* **2020**, *10*, 2544−2555.

(42) Wang, N.; Li, J.; Sun, W.; Hou, Y.; Zhang, L.; Hu, X.; Yang, Y.; Chen, X.; Chen, C.; Chen, B.; Qian, W. Rational Design of Zinc/Zeolite Catalyst: Selective Formation of p-Xylene from Methanol to Aromatics Reaction. *Angew. Chem., Int. Ed.* **2022**, *61*, e202114786.

(43) Xiao, J.; Cheng, K.; Xie, X.; Wang, M.; Xing, S.; Liu, Y.; Hartman, T.; Fu, D.; Bossers, K.; van Huis, M. A.; van Blaaderen, A.;

Wang, Y.; Weckhuysen, B. M. Tandem catalysis with double-shelled hollow spheres. *Nat. Mater.* **2022**, *21*, 572−579.

(44) Wang, C.; Zhang, J.; Qin, G.; Wang, L.; Zuidema, E.; Yang, Q.; Dang, S.; Yang, C.; Xiao, J.; Meng, X.; Mesters, C.; Xiao, F.-S. Direct Conversion of Syngas to Ethanol within Zeolite Crystals. *Chem* **2020**, *6*, 646−657.

(45) Zhang, J.; Wang, L.; Zhang, B.; Zhao, H.; Kolb, U.; Zhu, Y.; Liu, L.; Han, Y.; Wang, G.; Wang, C.; Su, D. S.; Gates, B. C.; Xiao, F.-S. Sinter-resistant metal nanoparticle catalysts achieved by immobilization within zeolite crystals via seed-directed growth. *Nat. Catal.* **2018**, *1*, 540−546.

(46) Han, S.; Linares, N.; Terlier, T.; Hoke, J. B.; García Martínez, J.; Li, Y.; Rimer, J. D. Cooperative Surface Passivation and Hierarchical Structuring of Zeolite Beta Catalysts. *Angew. Chem., Int. Ed.* **2022**, *61*, e202210434.

(47) Le, T. T.; Shilpa, K.; Lee, C.; Han, S.; Weiland, C.; Bare, S. R.; Dauenhauer, P. J.; Rimer, J. D. Core-shell and egg-shell zeolite catalysts for enhanced hydrocarbon processing. *J. Catal.* **2022**, *405*, 664−675.

(48) Gao, W.; Guo, L.; Wu, Q.; Wang, C.; Guo, X.; He, Y.; Zhang, P.; Yang, G.; Liu, G.; Wu, J.; Tsubaki, N. Capsule-like zeolite catalyst fabricated by solvent-free strategy for para-Xylene formation from CO$_2$ hydrogenation. *Appl. Catal. B* **2022**, *303*, 120906.

(49) Li, T.; Roy, K.; Krumeich, F.; Artiglia, L.; Huthwelker, T.; Bokhoven, J. A. Variation of Aluminium Distribution in Small-Sized ZSM-5 Crystals during Desilication. *Chem. − Eur. J.* **2019**, *25*, 15879−15886.

(50) Boronat, M.; Corma, A. What Is Measured When Measuring Acidity in Zeolites with Probe Molecules? *ACS Catal.* **2019**, *9*, 1539−1548.

(51) Gu, F.; Li, C.; Han, D.; Wang, Z. Manipulating the Defect Structure (VO) of In$_2$O$_3$ Nanoparticles for Enhancement of Formaldehyde Detection. *ACS Appl. Mater. Interfaces* **2018**, *10*, 933−942.

(52) Li, J.; Zhang, M.; Guan, Z.; Li, Q.; He, C.; Yang, J. Synergistic effect of surface and bulk single-electron-trapped oxygen vacancy of TiO$_2$ in the photocatalytic reduction of CO$_2$. *Appl. Catal. B* **2017**, *206*, 300−307.

(53) Ziemba, M.; Radtke, M.; Schumacher, L.; Hess, C. Elucidating CO2 Hydrogenation over In2O3 Nanoparticles using Operando UV/Vis and Impedance Spectroscopies. *Angew. Chem., Int. Ed.* **2022**, *61*, e202209388.

(54) Lee, C. H.; Kim, M.; Kim, T.; Kim, A.; Paek, J.; Lee, J. W.; Choi, S.-Y.; Kim, K.; Park, J.-B.; Lee, K. Ambient Pressure Syntheses of Size-Controlled Corundum-type In$_2$O$_3$ Nanocubes. *J. Am. Chem. Soc.* **2006**, *128*, 9326−9327.

(55) Hamberg, I.; Granqvist, C. G. Theoretical model for the optical properties of In$_2$O$_3$: Sn films in the 0.3−50 μm range. *Sol. Energy Mater.* **1986**, *14*, 241−256.

(56) Fu, D. L.; Paioni, A. L.; Lian, C.; van der Heijden, O.; Baldus, M.; Weckhuysen, B. M. Elucidating Zeolite Channel Geometry-Reaction Intermediate Relationships for the Methanol-to-Hydrocarbon Process. *Angew. Chem., Int. Ed.* **2020**, *59*, 20024−20030.

(57) Fu, D.; van der Heijden, O.; Stanciakova, K.; Schmidt, J. E.; Weckhuysen, B. M. Disentangling Reaction Processes of Zeolites within Single-Oriented Channels. *Angew. Chem., Int. Ed.* **2020**, *59*, 15502−15506.

(58) Yarulina, I.; De Wispelaere, K.; Bailleul, S.; Goetze, J.; Radersma, M.; Abou-Hamad, E.; Vollmer, I.; Goesten, M.; Mezari, B.; Hensen, E. J. M.; Martínez-Espín, J. S.; Morten, M.; Mitchell, S.; Perez-Ramirez, J.; Olsbye, U.; Weckhuysen, B. M.; Van Speybroeck, V.; Kapteijn, F.; Gascon, J. Structure−performance descriptors and the role of Lewis acidity in the methanol-to-propylene process. *Nat. Chem.* **2018**, *10*, 804−812.

(59) Dai, H.; Shen, Y.; Yang, T.; Lee, C.; Fu, D.; Agarwal, A.; Le, T. T.; Tsapatsis, M.; Palmer, J. C.; Weckhuysen, B. M.; Dauenhauer, P. J.; Zou, X.; Rimer, J. D. Finned zeolite catalysts. *Nat. Mater.* **2020**, *19*, 1074−1080.

(60) Peng, S.; Gao, M.; Li, H.; Yang, M.; Ye, M.; Liu, Z. Control of Surface Barriers in Mass Transfer to Modulate Methanol-to-Olefins Reaction over SAPO-34 Zeolites. *Angew. Chem., Int. Ed.* **2020**, *59*, 21945−21948.

(61) Liang, T.; Chen, J.; Qin, Z.; Li, J.; Wang, P.; Wang, S.; Wang, G.; Dong, M.; Fan, W.; Wang, J. Conversion of Methanol to Olefins over H-ZSM-5 Zeolite: Reaction Pathway Is Related to the Framework Aluminum Siting. *ACS Catal.* **2016**, *6*, 7311−7325.

(62) Shen, Y. F.; Le, T. T.; Fu, D. L.; Schmidt, J. E.; Filez, M.; Weckhuysen, B. M.; Rimer, J. D. Deconvoluting the Competing Effects of Zeolite Framework Topology and Diffusion Path Length on Methanol to Hydrocarbons Reaction. *ACS Catal.* **2018**, *8*, 11042−11053.

(63) Mores, D.; Kornatowski, J.; Olsbye, U.; Weckhuysen, B. M. Coke Formation during the Methanol-to-Olefin Conversion: In Situ Microspectroscopy on Individual H-ZSM-5 Crystals with Different Bronsted Acidity. *Chem. − Eur. J.* **2011**, *17*, 2874−2884.

(64) Arora, S. S.; Nieskens, D. L. S.; Malek, A.; Bhan, A. Lifetime improvement in methanol-to-olefins catalysis over chabazite materials by high-pressure H$_2$ co-feeds. *Nat. Catal.* **2018**, *1*, 666−672.